Self-organisation of planar and tripod-shaped DNA stars confined to the water–air interface

Clemens Jochum, Nataša Adžić, Emmanuel Stiakakis, Gerhard Kahl & Christos N. Likos

Published online: 04 Mar 2025.

Submit your article to this journal ↗

View related articles ↗

View Crossmark data ↗

Taylor & Francis
Taylor & Francis Group

THERMODYNAMICS 2024 CONFERENCE (BY INVITATION ONLY)

Check for updates

Self-organisation of planar and tripod-shaped DNA stars confined to the water–air interface

Clemens Jochum[a], Nataša Adžić [b,c], Emmanuel Stiakakis [d], Gerhard Kahl[a] and Christos N. Likos [c]

[a]Institute for Theoretical Physics, TU Wien, Vienna, Austria; [b]Institute of Physics Belgrade, University of Belgrade, Belgrade, Serbia; [c]Faculty of Physics, University of Vienna, Vienna, Austria; [d]Biomacromolecular Systems and Processes, Institute of Biological Information Processing (IBI-4), Forschungszentrum Jülich, Jülich, Germany

ABSTRACT
Using molecular dynamic simulations of coarse-grained models, we study the self-organisation of star-shaped all-DNA constructs, composed of suitably intertwined single-stranded DNA chains, confined to water–air interface. Two configurations of DNA stars are considered: planar and tripod with respect to whether the entire star is fixed to an interface or only its terminating nucleotides, while the rest is allowed to dive into a water where high concentration of monovalent salt is dissolved. Calculated structural properties of the solutions they form as well as their dynamical features, investigated in a range from low- to intermediate densities, reveal that both systems stay in liquid state maintaining remarkably similar properties despite striking differences in the conformation of the composing molecules.
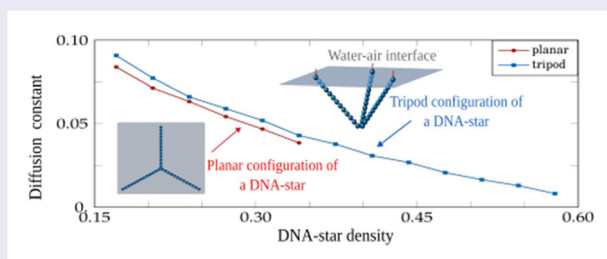
1. Introduction

The bottom-up approach for surface nano-patterning relies on the self-assembly of two-dimensional confined building blocks. Among the available building materials in this emerging field, DNA holds great promise for the realisation of nano-structured surfaces with arbitrary complexity and spatial addressability at the subnanometer level [1–8], which are of relevance in molecular [9–11] and cellular biophysics [12–14] and materials science [15–17]. Various strategies have been employed for long-range patterning of self-assembled all-DNA nanostructures (DNA tiles and DNA origami structures) on solid substrates [18]. The interfacing of DNA structures with hard surfaces has been achieved in numerous ways, including surfaces that actively influence DNA assembly (such as mica) [19] and selective adsorption on lithographically patterned surfaces [20], which is a characteristic example of a synergy between bottom-up and top-down fabrication approaches and DNA confinement onto fluid-like two-dimensional (2D) surfaces such as lipid bilayers [21]. The latter type of DNA adsorption can be achieved either by electrostatic binding on an oppositely charged cationic lipid bilayer [22,23] or by a combination of a hydrophobic-mediated DNA anchoring and electrostatic DNA binding to these membranes [24]. The main advantage of this 2D DNA confinement approach over the above-mentioned strategies is that these fluidic 2D surfaces can effectively interface DNA with spherical and planar solid substrates, allowing DNA nanostructures to diffuse freely in-plane. The critical role of the surface-mediated diffusion in the long-range organisation of DNA nano-structures with controlled lateral interactions has been demonstrated, revealing that DNA origami structures [22,23] and star-shaped crossover DNA tiles [24] can self-assemble into a rich assortment of micrometer-sized surface packing morphologies.

CONTACT Nataša Adžić ✉ natasa.adzic@ipb.ac.rs 📧 Institute of Physics Belgrade, University of Belgrade, Pregrevica 118, Belgrade RS-11080, Serbia; Faculty of Physics, University of Vienna, Boltzmanngasse 5, Vienna A-1090, Austria

From the experimental point of view, the most common tool to access the static structure of these all-DNA 2D assemblies is atomic force microscopy (AFM). A far more difficult task is to probe dynamic processes involved in the formation of these assemblies. High-speed AFM imaging [23] and noninvasive super-resolution microscopy [25] experiments seem to be a promising tool for the direct visualisation of the self-assembly process, however, access to local and fast processes such as the mean squared displacement of the centre of the mass of the adsorbed DNA nanostructures is a major experimental challenge. Molecular dynamics (MD) simulations could be a complementary tool offering structural and dynamical information in an unprecedented level of detail.

Here, we investigate the properties of concentrated adsorbates of a structurally simple yet rich all-DNA construct, the so-called Y-shaped all-DNA [26], i.e. a DNA-based three-arm star. To this end, we employ computer simulation in order to gain a detailed information about DNA-star assemblies confined to an interface. This DNA entity is a three-armed star, consisting of double-stranded helices, 13 base-pairs long, as shown in Figure 1(a), formed in synthesis via hybridisation of three single-stranded DNA chains. Each of these DNAs has partially complementary sequences to the other two DNA chains, leading thus to the formation of base-pairs along the arms. The Y-shaped DNA nanostructure has been used as a building block for the controlled assembly of novel all-DNA dendritic structures [27]. These novel macromolecules have been modelled in computer simulations [28] *via* a simple bead-spring model, proposed in the context of polyelectrolyte brushes [29,30]. In this contribution, we rely on the proposed model, which was also tested experimentally (see Ref. [28]) for Y-shaped DNA star as well as for higher generations of all- DNA dendrimers with rigid or flexible connecting bonds between the successive generations [31]. Hence, we investigate the self-assembly of all-DNA stars using the tested model, where the each base-pair is represented by a single monomer bead (see Figure 1(b)), which interacts with neighbouring ones via the interactions that recover structural properties of double-stranded DNAs (see also Appendix).

Considering a 2D ensemble of these DNA-stars confined to a water–air interface, we study two different scenarios: one where we have assumed that *all* base-pairs are fixed to an air-water interface, termed the 'planar configuration' and shown in Figure 1(b), and the other where the only terminating beads of each arm are fixed to this interface, allowing thus the central monomer of the star to 'dive' into the water, termed the 'tripod configuration' and shown in Figure 1(c). Particular static and dynamic properties that we have calculated from our simulations, enable us to spot out the characteristic differences between the two scenarios.

Experiments confirmed the importance of a role of DNA stars in the formation of gels [32], liquid crystals [33], cluster crystals [34] in bulk solution. Particularly the bulk solution of 3-arms DNA stars with sticky ends
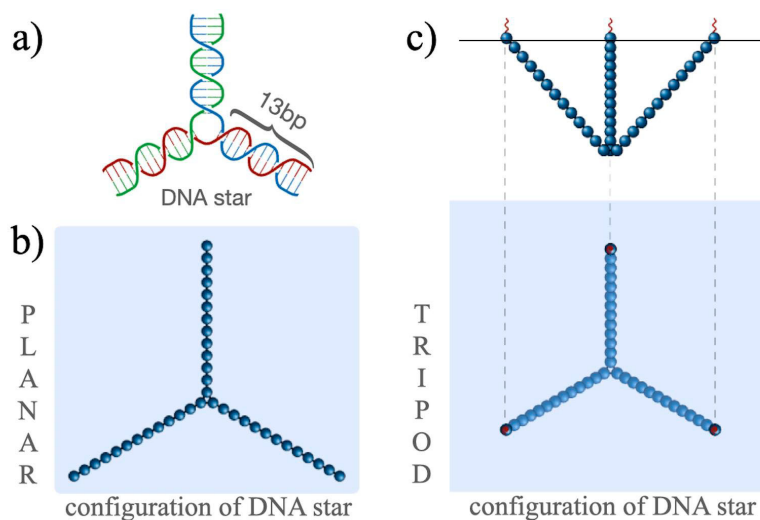

Figure 1. Schematic sketches of: (a) a three-arm DNA star composed of double-stranded helices 13 base-pairs long; and the two configurations it can take when confined to an interface (b) the planar configuration and (c) the tripod configuration with the tip immersed into the fluid. Monomer beads stand for base pairs along DNA strands (not drawn to scale) whereas the blue plane represents the interface to which the macromolecules are confined. In the tripod configuration the ends of the arms of the DNA star are attached to the interface *via* amphiphilic units, depicted by the red appendices, while in the planar configuration the entire DNA star is fixed to the interface *via* amphiphilic units (not shown).

is studied in simulations [35] and in experiment [32] and it is shown that system stays in a disordered state for a wide range of DNA star concentration and temperatures. Concerning all-DNA organisation in two-dimensional confinement, the self-organisation of DNA motifs has also been investigated experimentally [36] showing how DNA tiles can be used for constructing 2D lattices with programmable features of nanometer precision. Nevertheless, the experimental verification of results for the system at hand is still lacking.

In this paper we provide a general description of the model accompanied with details of the set up for the molecular dynamics simulation we use to study two systems of DNA stars confined at the interface, given in Appendix. Section 2 is dedicated to a detailed presentation of the static and of the dynamic properties of the DNA stars in planar and in the tripod configurations respectively. The obtained results for the two aforementioned scenarios are then directly compared with one another. The work is supplemented with results for the effective interactions of the DNA-stars in the planar configuration, given in Section 3, where we discuss how it compares with the data provided in the literature on a closely related model.

2. DNA stars in planar and tripod configurations

As specified in the Introduction, we study self-assembly of DNA stars at water–air interface, focusing on two types of DNA star solutions: one composed of all-DNA stars in planar configuration, Figure 1(b), and the other consisting of all-DNA stars in tripod configuration, Figure 1(c). In experiments, the flat configuration is achieved *via* amphiphilic units [37,38] that decorate DNA chains, so that the whole star is fixed to the surface. For the tripod configuration, amphiphilic units are attached only at the end of the arms, fixing the terminating beads to the interface, Figure 1(c), while the remaining parts of the star are able to dive into the water solution with dissolved monovalent salt. In our model, these amphiphilic units are not considered explicitly. Instead, we fix the star to the interface simply by setting the vertical coordinate of all beads to zero in the case of flat DNA stars while in the case of tripod system only the end monomers are confined to $z = 0$ plane, matching the vertical position of the interface and allowing other monomers to dive into the solvent. The interface itself is not simulated explicitly but is provided by the introduced confinement. DNA stars in both configurations are allowed to move freely in the lateral direction. We employ the same coarse-grained bead-spring model for the DNA stars in both configurations, as stated in Introduction, modelling each base-pair as spherical unit, resulting in a sequence of 13 monomers

per arm of the star whose length amounts to $\simeq 44$ Å. Each monomer interacts with the neighbouring beads with different types of interactions that mimic structural properties of DNA double strand. Salt ions are treated implicitly via a Debye screening parameter. The numerical values of parameters for each potential employed are given in Appendix (for more details see also [28,30]). In our system, DNA helices have blunt ends in contrast to that of Ref. [28], where the arms are terminated with the short sequence of the single-stranded DNA chains that were used as linkers between stars for building higher generation of dendrimers.

The density of 2D solutions of DNA stars is characterised by the (planar) packing fraction,

$$\eta_s = 2\pi R_g^2 \rho_d \quad \text{with } \rho_d = \frac{N_d}{A}. \quad (1)$$

Here, R_g is the radius of gyration of the DNA star. For the flat configuration, it takes the value $R_g = 25.5$ Å. The same value is used for the densities of the tripod system for the reason of an unambiguous comparison of corresponding quantities that follow. Moreover, the stars in the tripod configuration take the planar shape at low star densities. In the above relation, ρ_d is the number density, N_d is the number of stars in a given area A. As discussed in the subsequent subsections, we considered η_s-values up to 0.57. For simplicity, we assume that the permittivity in both media is the same as the stars remain, due to their hydrophilicity, slightly below the interface, in water with dissolved salt of concentration $c = 100$ mM, which represents a typical experimental salinity.

In order to investigate the properties of our systems we have performed standard molecular dynamics simulations in the canonical ensemble, using a Langevin thermostat, fixing the temperature to room conditions, $T = 298$ K and applying the periodic boundary conditions in x and y directions only. We have used the software package `ESPResSo` [39]. Throughout, ensembles of 400 DNA stars have been considered, corresponding to $400 \times 13 \times 3 = 15600$ monomeric beads. MD simulations were extended over 10^8 time steps, corresponding thus to a total, macroscopic time of 0.25 μs (for more details see Appendix). Simulation snapshots for low- and mid-DNA star densities, η_s are shown in Figure 2, for both types of solution – one composed of planar DNA stars (a) and (b) and one consisting of tripod star configuration (c) and (d).

2.1. Systems of planar DNA stars

To study planar (*flat*) all-DNA stars confined to the interface, monomer-resolved MD simulations are performed for the interface density of the DNA stars, η_s, as defined
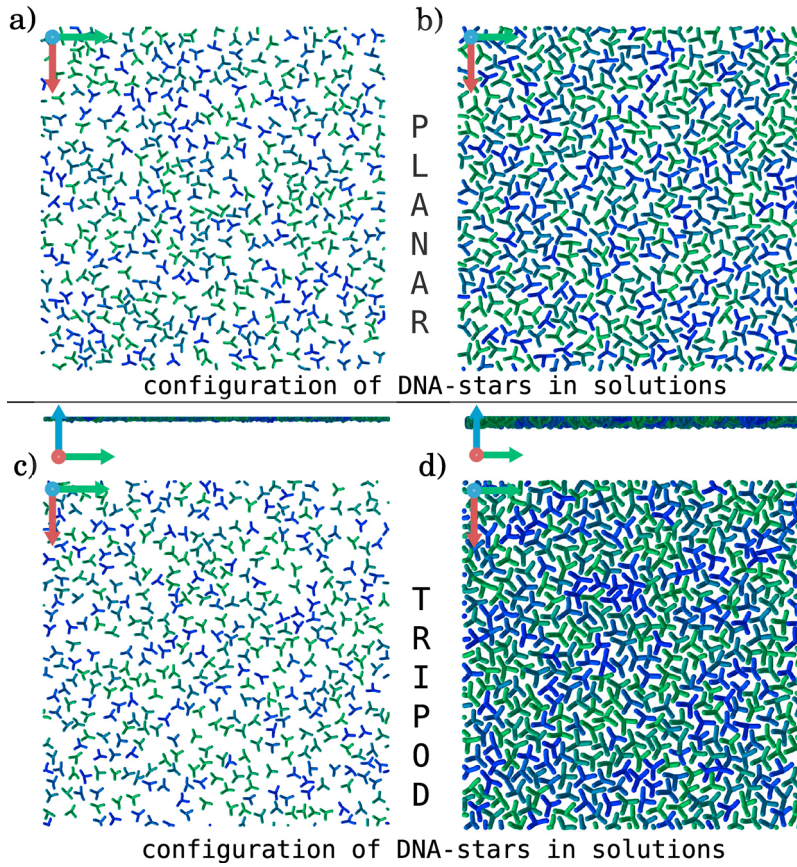
Figure 2. Simulation snapshots of bulk DNA stars solutions confined at the air-water interface at salt concentration $c = 100\,\text{mM}$ and DNA stars' densities (a) $\eta_s = 0.17$ and (b) $\eta_s = 0.34$ for the planar configurations of stars and (c) $\eta_s = 0.17$ and (d) $\eta_s = 0.54$ for the tripod configuration of stars. DNA stars are shown in different colours in order to increase distinguishability between them. The upper panels in (c) and (d) stand for the projection of the simulation box in the yz-plane, whereas the bottom panels show the projection on xy-plane. The orientations of the x-, y- and z-axis are indicated by the red, green and blue arrows, respectively.

in Equation (1) between 0.17 and 0.34. Already for intermediate densities (i.e. for $\eta_s \simeq 0.25$) the particular shape of the stars renders the construction of the initial configurations very challenging. To avoid an overlap of the arms, the stars have to be arranged for their initial configuration in a particularly chosen geometric pattern. With such ordered arrangements one might even proceed to higher η_s-values; however, at these high densities the system would never be able to equillibrate but would rather remain in a trapped configuration. For this reason, we have limited our investigations on the flat stars to $\eta_s \leq 0.34$.

In Figure 3(a), we show the pair correlation function, $g_{yy}(r)$, of our two-dimensional system of flat DNA stars, where r represents the centre-of-mass distance, r_{com}. We find for $g_{yy}(r)$ the typical shape encountered for correlation functions of a disordered state: a main peak with subsequent oscillations, which become more pronounced as the density increases. The distance of closest approach (i.e. below which $g_{yy}(r)$ essentially vanishes) is located at $r \simeq 50\,\text{Å}$, which corresponds to the length of one arm of the stars. This feature indicates that as a consequence of

the two dimensional confinement, the DNA stars hardly penetrate. The position of the maximum in $g_{yy}(r)$ moves to smaller values with increasing η_s, as expected.

The information about the static structure of the system is supplemented by dynamic properties: to this end we have calculated the mean squared displacement (MSD), denoted by

$$\text{MSD}(\Delta t) = \langle (\Delta \mathbf{r}_{\text{com}}(\Delta t))^2 \rangle$$
$$= \langle (\mathbf{r}_{\text{com}}(t + \Delta t) - \mathbf{r}_{\text{com}}(t))^2 \rangle, \quad (2)$$

where a DNA star is considered to be located at its centre-of-mass, $\mathbf{r}_{\text{com}}$. Averaging the one-particle correlation function independently over each macromolecule and using gliding time windows we can achieve a sufficiently high numerical accuracy of the data. Results for the MSD, calculated for densities within the aforementioned density window, are shown in Figure 3(b) on a double logarithmic scale. At larger times we find a neat diffusive behaviour, where different vertical shifts, corresponding to decreasing diffusion coefficients, are found for different η_s-values, see discussion in the following
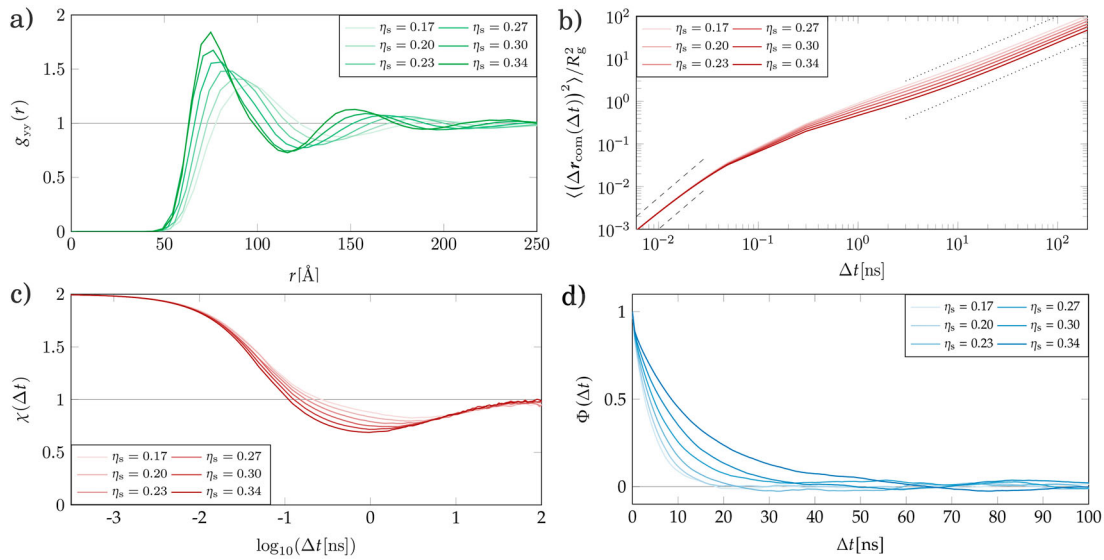
Figure 3. (a) Radial distribution function $g_{yy}(r)$ of a system of planar DNA stars, plotted as a function of centre-of-mass separation r, given in units of Å. (b) Mean squared displacement (MSD) $\langle(\Delta \mathbf{r}_{com}(\Delta t))^2\rangle$ of the centres-of-mass, $\mathbf{r}_{com}(t)$ of DNA stars in the flat configuration, given in units of R_g^2, as a function of the time lag Δt, given in ns. The dashed lines highlight the ballistic regime (i.e. MSD $\propto t^2$), while the dotted lines indicate the diffusive regime (i.e. MSD $\propto t$). (c) Local logarithmic derivative, $\chi(\Delta t)$, of the MSD, related to the centres-of-mass, $\mathbf{r}_{com}(t)$, of DNA stars in the flat configuration, given in units of the squared radius of gyration R_g^2, as a function of the logarithmic time lag. (d) Normalised 'orientational' time auto-correlation function $\Phi(\Delta t)$ of DNA stars in the flat configurations as a function of lag time Δt, given in ns. Results are shown for different values of surface density η_s, as labelled.

subsection. To elucidate a possibly sub-diffusive regime, we have calculated the logarithmic derivative of the MSD, $\chi(\Delta t)$, defined *via*

$$\chi(\Delta t) = \frac{d[\log_{10}\langle(\mathbf{r}_{com}(t+\Delta t)-\mathbf{r}_{com}(t))^2\rangle]}{d[\log_{10}\Delta t]} \quad (3)$$

The quantity $\chi(\Delta t)$ is shown in Figure 3(c). We find that this function deviates for $10^{-1}\,\mathrm{ns} \leq \Delta t \leq 10^2\,\mathrm{ns}$ from the diffusive behaviour when $\chi(\Delta t)$ assumes values smaller than unity: there, $\chi(\Delta t)$ ranges between $\simeq 0.8$ (for low densities) to $\simeq 0.6$ (at intermediate densities). Obviously, in the latter case, the star-like architecture of the macromolecules renders the system rather bulky, leading to a more pronounced sub-diffusive behaviour than at low densities, where the macromolecules can move around more freely.

Finally, we have investigated the orientational dynamics of the DNA stars, by calculating the (normalised) auto-correlation function of the orientation of the DNA arms. To this end, we have tagged an arbitrarily chosen arm in each DNA star and have connected the centre-of-mass of the star with the end monomer of the same arm *via* the vector $\mathbf{a}(t)$. The orientational correlation function is then given at a lag time Δt by the function $\Phi(\Delta t) = \langle\mathbf{a}(t)\cdot\mathbf{a}(t+\Delta t)\rangle$. The results for the auto-correlation function, obtained *via* a similar averaging procedure as the one mentioned above for the MSD,

are shown in Figure 3(d) for different values of surface density η_s. As expected, the decay of this function is strongly density-dependent: for instance, for the smallest density $\eta_s = 0.17$ and the largest density $\eta_s = 0.34$, the auto-correlation of $\mathbf{a}(t)$ vanishes at lag times ns and ns, respectively. In both cases, at these lag times, the DNA stars have propagated over a distance of only $4R_g$, see Figure 3(b). This finding provides evidence that in this system the orientational correlations decay considerably faster than the spatial correlations.

2.2. Systems of tripod DNA stars

MD simulations have been performed to investigate all-DNA stars in the tripod configuration confined to a water–air interface. The salt concentration was assumed to be mM as before. Due to the ability of these DNA stars to immerse their tip (*i.e.* central junctions of the stars) into the fluid, interface densities up to $\eta_s = 0.58$ could now be considered. The z-components of the tips of the tripods in the initial configuration were forced to assume rather large values, rendering thereby the triangular area formed by the end monomers of the arms much smaller (as compared to the case of flat, extended DNA stars). In that way congestion is avoided.

In Figure 4(a), we show the pair correlation function $g_{yy}(r)$ of the system where the distance between two
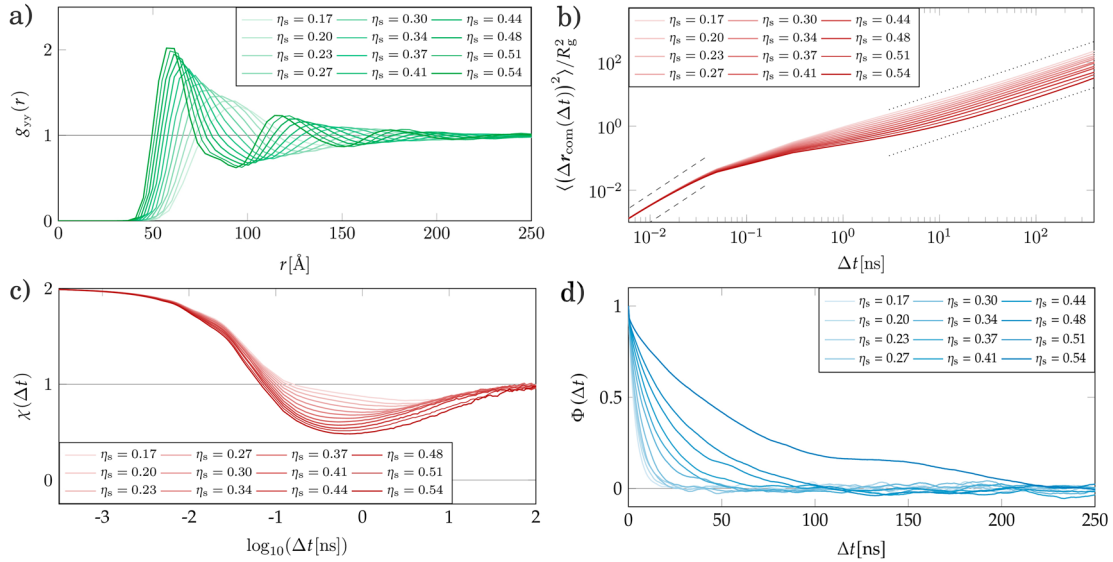
Figure 4. (a) Radial distribution function $g_{yy}(r)$ for the system of DNA stars in the tripod configuration, plotted as a function of the centre-of-mass separation r, given in units of Å. (b) Mean squared displacement (MSD) of the centres-of-mass, $\mathbf{r}_{com}(t)$ of DNA stars in the tripod configuration, given in units of R_g^2, as a function of the time lag Δt, given in ns. The dashed lines highlight the ballistic regime (i.e. MSD $\propto t^2$), while the dotted lines indicate the diffusive regime (i.e. MSD $\propto t$). (c) Logarithmic derivative, $\chi(\Delta t)$, of the MSD related to the centres-of-mass, $r_{com}(t)$, of DNA stars in the tripod configuration, given in units of the squared radius of gyration R_g^2, as a function of logarithmic time lag. (d) Normalised orientational time auto-correlation function $\Phi(\Delta t)$ of DNA stars in the tripod configurations as a function of lag time Δt, given in ns. Results are shown for different values of surface density η_s, as labelled.

stars, now refers to the projection of the tips onto the interface. Similar to the case of flat DNA stars we find correlation functions which characterise a disordered, fluid state; only for the highest packing fractions one can find minute fingerprints of an evolving side-shoulder of the main peak, close to the first minimum, a feature which might be considered as a precursor of a possible super-cooled state [40–42]. If we consider again the distance beyond which $g_{yy}(r)$ is non-zero, we find a value below 50 Å, providing evidence that in the tripod configuration the DNA stars are able to approach each other more closely than in the case of flat stars. The positions of the maxima in $g_{yy}(r)$ show the expected shift to smaller distances with increasing η_s.

In analogy to the previous subsection we investigated the dynamic translational and orientational correlations by calculating the MSD (now related to the projections of the tips onto the interface), the logarithmic derivative of the MSD, $\chi(\Delta t)$ and the orientational auto-correlation functions $\Phi(\Delta t)$ of the arm vectors $\mathbf{a}(t)$ as functions of the time lag Δt. The results are shown in Figure 4(b–d), respectively, which now extend over a considerably larger range of densities. For each of these functions, findings similar to those made for the planar configuration hold true. The direct comparison of the results obtained for the aforementioned functions, in the the planar and in the tripod configurations is presented in the following subsection.

In contrast to the planar DNA stars, the marco-molecules in the tripod configuration possess additional degrees of freedom: the vertical position of the central junction of the star Δz, the angle enclosed by the arms and the interface ξ, and the angles formed between the arms θ_i, see the inset of the Figure 5(a).

We calculated the probability distribution $P(\Delta z)$ of the immersion depth of the tip of the stars, Δz (which is simply the orthonormal distance of the central junction from the interface), Figure 5(a), and the probability distribution $P(\xi)$ of the angle ξ (which is enclosed by the arms of the star and the interface), Figure 5(b), for different densities. For a given density η_s, $P(\Delta z)$ and $P(\xi)$ are very similar in their shape, a fact which is imposed by the geometry of the tripod configuration. We find a striking change in shape of these functions as the density increases. According to the shape of the distributions we can clearly separate three density regimes: at small densities we find a pronounced peak for rather small Δz values ($\Delta z \simeq 8$ Å) and ξ-values located at $\xi \simeq 0.05\pi \simeq 10°$: here the majority of the stars show a clear preference for rather flat tripod configurations, made possible by the ample space available at small densities. At high densities, we find again pronounced peaks in the two distributions (for $\Delta z \simeq 25$ Å and $\xi \simeq 0.2\pi \simeq 36°$); in this context it must be noted (i) that the length of one star arm amounts approximately to 44 Å (to be compared to the aforementioned value of Δz) and (ii) that the steric repulsion
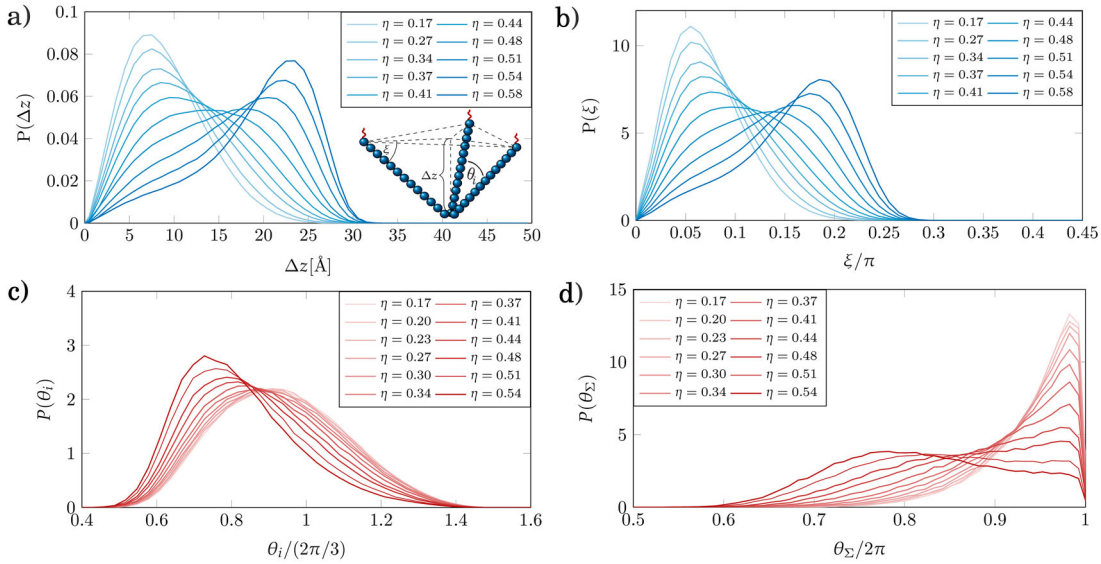
Figure 5. Probability distributions of characteristic length and angles of the tripod DNA star configuration (as indicated at the inset (a)), i.e. (a) P(Δz) as a function of the immersion depth Δz given in Å. (b) P(ξ) as a function of the arm-interface angle ξ given in units of π. (c) P(θ_i) as a function of the interarm angles θ_i ($i = 1, 2, 3$) given in units of $2\pi/3$. The distributions P(θ_i) represent the cumulative results over all three interarm angles θ_i, $i = 1, 2, 3$. (d) Probability distribution P(θ_Σ) as a function of the sum over the interarm angles, θ_Σ given in units of 2π. Results are plotted for different values of the surface density η_s, as labelled. The probability distributions are normalised via: $\int_0^\infty P(\Delta z)\, d(\Delta z) = 1$; $\int_0^{\pi/2} P(\xi)\, d\xi = 1$; $\int_0^\pi P(\theta_i)\, d\theta_i = 1$ and $\int_0^{2\pi} P(\theta_\Sigma)\, d\theta_\Sigma = 1$.

between the DNA arms does not allow angles ξ much larger than $\pi/4 = 45°$, corresponding to a vertical tip position of 31 Å. At high densities the tripods assume rather sharp tripod configurations, as a consequence of the reduced available space and the mutual repulsion between the stars. The most interesting effects can be found in the intermediate density regime (i.e. around $\eta_s \simeq 0.44$) where both distributions extend over a broad range of the respective variables: to be more specific, a broad 'maximum plateau' extends over $\simeq 8$ Å (in Δz) and over $\simeq 0.08\pi \simeq 14°$ (in ξ) which does not allow to identify a preferred tripod configuration in terms of Δz and ξ. Instead, a large variety of preferred star conformations can be identified. Undoubtedly, in this density range the DNA stars also interpenetrate, and the effects are a consequence of a strong interplay between space optimisation (wide space offered between the arms for interpenetration) on the one hand and mutual repulsion between the end beads of the arms, on the other hand.

Finally, the deviation of DNA stars from the planar configuration can also be analysed via the interarm angles θ_i, with $i = 1, 2, 3$, and their sum θ_Σ. The corresponding probability distributions P(θ_i) with $i = 1, 2, 3$ and P(θ_Σ) are shown in Figure 5(c ,d). θ_Σ shows a pronounced peak at low densities for $\theta_\Sigma \simeq 2\pi = 360°$ and P(θ_i) has a maximum slightly smaller than $2\pi/3 = 120°$, corroborating the emergence of predominantly flat star configurations. At high densities, on the other hand, θ_Σ shows a flat, but well-identifiable maximum for

$\simeq 0.78(2\pi) \simeq 280°$, while P($\theta_i$) has a well pronounced maximum for $\simeq 0.75(2\pi/3) \simeq 90°$. In the range of intermediate densities P(θ_Σ) is very broad, indicating that a large variety of tripod configurations can be identified in the system.

To obtain more insights into the conformational changes of the DNA stars as the density is increased, we introduce the concept of a *local* density, η_{loc}: this quantity is defined as the star density within a circular area of radius $r_{loc} = 200$ Å (corresponding to roughly 4.5 arm lengths), centred at the projection of the tip of the star onto the interface. In this manner, we obtain a quantitative information about the density fluctuations in a system of given *global* surface density, η_s. The probability distribution of η_{loc}, P(η_{loc}), is shown in Figure 6(a) for each of the global densities η_s of the tripod systems investigated. We see that the distributions are very similar in their shape for the different η_s: all of them are centred at the respective η_s-values and have a rather narrow half-width ($\simeq 0.05$), indicating that the local density varies only moderately around the value of the global density. With the concept of the local density in mind, we can now re-consider the immersion depth Δz and analyse it as a function of η_{loc}: in this context, it should be emphasised that – due to the considerable overlap of the P(η_{loc}), obtained for different global densities η_s (see Figure 6(a)) – data for a given value of the local density can now originate from simulations carried out for systems with different η_s-values. The corresponding data are shown
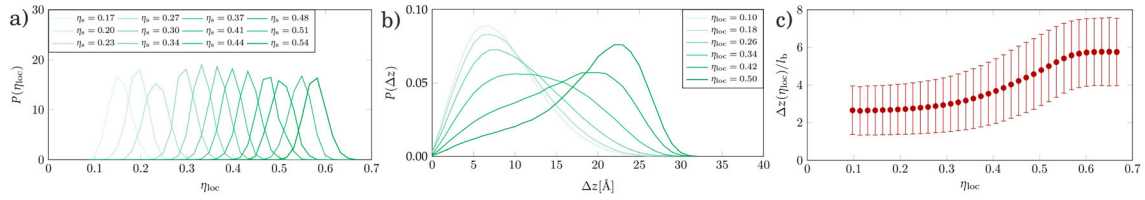
Figure 6. (a) Probability distribution P(η_{loc}) as a function of the *local* surface density, η_{loc}, of DNA stars in the tripod configuration. Results are plotted for different values of the *global* surface density η_s, as labelled. The probability distributions are normalised *via* $\int_0^\infty$ P(η_{loc}) dη_{loc} = 1. (b) Probability distribution P(Δz) as function of the immersion depth, Δz, of DNA stars in the tripod configuration; Δz is given in Å. Results are plotted for different values of the *local* surface density η_{loc}, as labelled. The probability distributions are normalised *via* $\int_0^\infty$ P(Δz) d(Δz) = 1. (c) Immersion depth Δz as function of the *local* surface density, η_{loc}, of DNA stars in the tripod configuration; Δz is given in units of l_b, i.e. equilibrium length of the harmonic bond, which for our model is given by l_b = 3.4 Å. The vertical bars represent the half-width of the distribution of the Δz.

in Figure 6(b ,c) over a representative range of η_{loc}. The probability distributions $P(\Delta z)$, plotted for different *local* densities – see Figure 6(b) – shows essentially the same shape as the related functions, plotted for different *global* densities η_s – see panel (a) of Figure 5. If we now display the tip position as a function of η_{local}, see Figure 6(c), we see that $\Delta z(\eta_{local})$ undergoes a sigmoidal transition from a rather small value of $\Delta z \simeq 2.3l_b$ (corresponding to the left peak in panel (b) of Figure 6) to a considerably larger value of $\Delta z \simeq 5.9l_b$ (corresponding to the right peak in the above-mentioned panel); l_b is the equilibrium length of the harmonic bond (see Appendix), which for our model is given by l_b = 3.4 Å. The monotonous increase of $\Delta z(\eta_{loc})$ as a function of η_{loc} provides evidence that it is essentially the local density around a given DNA tripod that imposes the actual value of its tip position.

2.3. Planar DNA stars vs. tripod DNA stars

In this subsection, we present a direct comparison of selected properties, calculated in the previous subsections for the planar, and the tripod configurations of DNA stars confined to the interface and highlight the impact of the additional degrees of freedom for the tripod systems. Of course, this analysis is only possible for surface densities up to η_s = 0.34.

In Figure 7(a), we present the comparison of the radial distribution functions, $g_{yy}(r)$. At the lowest density (η_s = 0.17) there is almost no differences between the two scenarios. At η_s = 0.34, only a minor difference arises indicated by ability of DNA stars in the tripod configuration to arrange closer at the confinement. For the highest investigated density we see a small shoulder close to the first minimum in the $g_{yy}(r)$ of the tripod system, reflecting the aforementioned precursor of a possible supercooled state.

We continue with the comparison of the translational and the rotational correlations as functions of time; these results are presented in Figure 7(b–d). These data reveal

that the differences in the dynamic properties between the two types of systems are marginal. The MSDs in Figure 7(b) shows, although hardly discernible, that flat DNA stars diffuse somewhat slower than the tripod ones. We find that the logarithmic derivative of the MSD displayed in Figure 7(c), provide evidence of only marginal differences between the two types of systems: for DNA stars in the planar configuration the transition from the ballistic to the diffusive regime is somewhat shallower, corresponding to a slightly less pronounced sub-diffusive behaviour. Also, the orientational auto-correlations of the arm vectors, $\mathbf{a}(t)$, shown in Figure 7(d), decay slightly slower for DNA stars in the flat configurations. The tripods at the highest density, η_s = 0.58 hardly reach the diffusive regime in the time-window simulated and they show signatures of slow dynamics and an incipient glassy state; also the orienational correlation function barely relaxes within the time window of 250 ns.

Finally, we have extracted the diffusion constant, D, from the MSD *via* the Einstein relation for both types of systems as a function of η_s. This quantity is shown in Figure 8. It can be concluded that in the tripod configuration the DNA stars are slightly more diffusive, which is due to their aforementioned ability to evade each other at the interface.

Summarising, it can be concluded that the results for the static and dynamic correlation functions are remarkably similar between the two types of systems, despite their striking difference in their conformations. The reason for an almost identical behaviour could be sought in the range of investigated packing fractions. Namely, the stars in planar configuration are investigated for densities up to only η_s = 0.34. In that range of densities the available space offers possibility to the DNA star in tripod configuration to spread and take more planar-like shape, which is confirmed by probability distribution functions, see Figure 5. The same figure suggests that the differences between two systems would most likely arise for higher packing fractions, η_s > 0.5 which is at the moment not
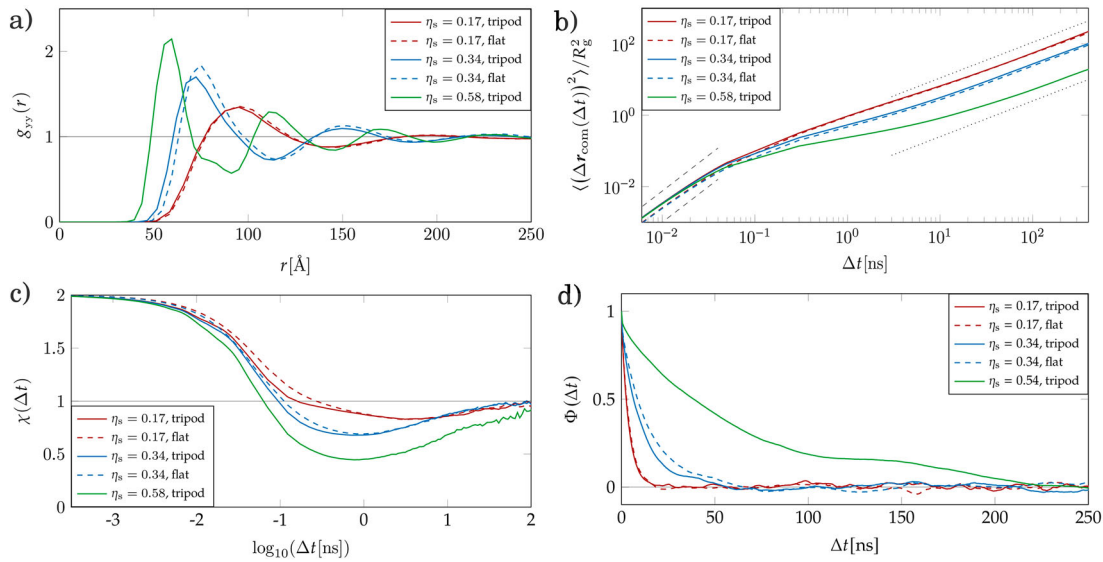
Figure 7. Comparing results between systems of DNA stars in the planar (dashed lines) and in the tripod (solid lines) configurations: (a) Radial distribution function $g_{yy}(r)$, plotted as a function of the centre-of-mass separation r, given in units of Å. (b) Mean squared displacement (MSD), given in units of R_g^2, as a function of the time lag Δt, given in ns. The dashed black lines highlight the ballistic regime (i.e. MSD $\propto t^2$), while the dotted black lines indicate the diffusive regime (i.e. MSD $\propto t$). (c) Logarithmic derivative, $\chi(\Delta t)$, of the MSD given in units of R_g^2, and as a function of the logarithm of time lag. (d) Normalised orientational time auto-correlation function $\Phi(\Delta t)$ for the star arm vector $\mathbf{a}(\Delta t)$ as a function of lag time Δt, given in ns. Results are shown for different values of surface density η_s, as labelled.
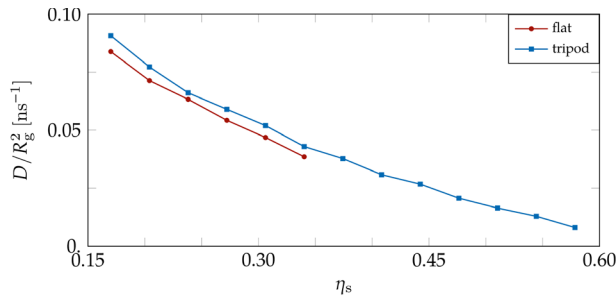

Figure 8. Diffusion constant of DNA stars, D, rescaled by R_g^2 and given in ns^{-1} as a function of the star density η_s. Results are compared between systems of DNA stars in the planar and in the tripod configuration, as labelled.

accessible for our full monomer-resolved simulations of solutions composed of planar DNA stars.

3. Effective interactions of planar DNA stars

To supplement results from the previous sections, we take into a consideration of additional insights to 2D DNA stars self-assembly. We calculate the effective potential between planar DNA stars. The analysis presented in the paper is based on the exact results calculated directly from the full monomer-resolved MD simulations and here we do not tend to use the approximative method of effective interactions to recover them. Instead, we aim to

corroborate the work of Velasco *et al.* [43], who calculated analytically the effective potential between planar Y-shaped DNA stars floating at the interface. The model they used (let us name it: *the reference model*) treats each arm of the DNA star as a stiff rod of the length corresponding to 13 base-pairs as it is the case in our system. Hence we use the Widom insertion (WI) method (see, e.g. [44,45]) to calculate the effective interaction between monomer-resolved model of DNA stars and we check how it compares to the analytical results from the reference model [43]. In both models, the dielectric jump between two interfacing areas is not considered and the stars are immersed in a water solution of the same salt concentration of $c = 100$ mM. It is important to emphasise the differences between the two models: one arises from the description of the charge along the arms – in the reference model it is considered as continuous, while it is discrete in monomer-resolved case; the other refers to the flexibility of the central junction of the star – namely in the reference model the angles enclosed between the rigid arms of the DNA stars were fixed to $\theta_i = \frac{2\pi}{3}i$, $i = 1, 2,$ 3 whereas in monomer-resolved model they are allowed to fluctuate. Therefore, in the following subsections, we introduce two types of planar monomer-resolved DNA stars: the one that we already studied in the main text which we will name here as *flat DNA star with flexible junction* and a modified version termed *flat DNA star with a rigid junction* where the angles θ_i are fixed

to match the scenario from the reference model. To gather the data for the related effective potential 2000 independent Widom insertions were performed for each system.

3.1. Planar DNA stars with rigid junction

In this subsection, we discuss our results obtained for the effective potential between two flat DNA stars with rigid junction, $\phi_{\text{eff}}(\alpha; \Delta x, \Delta y)$, which depends both on the inter-star vector, $\mathbf{r} = (\Delta x, \Delta y)$, and on the angle of rotation between the two stars, α, see Figure 9. Due to the symmetry, it is sufficient to limit the investigations to $0 \leq \alpha \leq 60°$. The vector $\mathbf{r}$ connects the centres-of-mass of the stars. We adjusted the respective system so that we consider only DNA stars with rigid (i.e. straight) arms, thus the interarm angles are fixed to $\theta_i = \frac{2\pi}{3}i$ ($i = 1$, 2, 3). This modification allows for a direct comparison between our numerical and the analytic approach [30]. Due to the high internal symmetry, the centre-of-mass of the star, $\mathbf{r}_{\text{com}}$, coincides with three central junction-monomers, $\mathbf{r}_{\text{cj}}$.

We have used the Widom insertion method [44] to calculate $\phi_{\text{eff}}(\alpha; \Delta x, \Delta y)$. Due to the rigidity of the stars, they do not contribute entropically to the effective potential, thus only one single Widom insertion per parameter set $\{\alpha, \Delta x, \Delta y\}$ is required to extract the interaction energy $\phi_{\text{eff}}(\alpha; \Delta x, \Delta y)$ between the two stars; nevertheless, we will keep for consistency's sake the label 'Widom insertion method'.

Results obtained for $\phi_{\text{eff}}(\alpha; \Delta x, \Delta y)$ via our numerical procedure (see Figure 10(b,d)) are compared in the following to data originating from the reference model [43], see Figure 10(a,c) at angles $\alpha = 0°$ and $\alpha = 60°$ as indicated at the panels. The potentials are shown both in

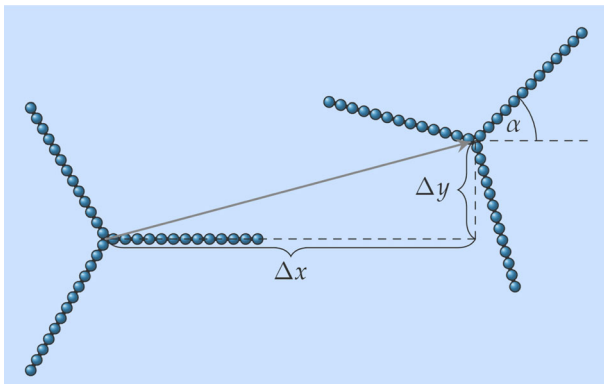two dimensional contour plots as well as in energy profiles, the latter ones being denoted by $\phi_{\text{eff}}(\alpha; \Delta r_i)$, with $i = 1, 2$, along selected slices through these energy landscapes; Δr_1 and Δr_2 are the respective slice coordinates. Additional results for slices through the related energy landscapes for $\alpha = 15°, 30°, 45°$ are shown in Figure 11.

Due to the three-fold rotational symmetry of the internal structure of the DNA stars we expect the effective potential $\phi_{\text{eff}}(\alpha; \Delta x, \Delta y)$ to exhibit a corresponding rotational symmetry. Indeed, all results display such a three-fold symmetry, as can be seen in panels (c) and (d) in Figure 10. For the angle $\alpha = 0°$ even a six-fold symmetry can be identified in the potential $\phi_{\text{eff}}(\alpha = 0°; \Delta x, \Delta y)$, see panels (a) and (b) of Figure 10. We note that the largest values for $\phi_{\text{eff}}(\alpha; \Delta x, \Delta y)$ can be expected for $\alpha = 0°$ and $\alpha = 60°$ due to the parallel alignment of one or more arms of the DNA stars and the resulting high probability for a considerable degree of overlap of the arms.

The comparison of the two sets of data for $\phi_{\text{eff}}(\alpha; \Delta x, \Delta y)$, calculated for $\alpha = 0°$ and $\alpha = 60°$, reflects, on one side differences in the features of the continuous and of the discrete models but provides, on the other side, evidence for a high degree of consistency of the two approaches. As a consequence of the constant charge density along the arms in the model used in Ref. [43], the effective potentials are smooth functions in their arguments, as can be seen both from the contour plots as well as from the energy profiles. In contrast, the effective interactions for the bead model, computed via the WI method clearly reflects the internal architecture of the arms, which are composed of essentially impenetrable spherical units: their strong repulsion at short distances is responsible for the pronounced peaks, located at the positions of each of these monomeric units. On the other hand, it can be seen that the peaks in the density profiles $\phi_{\text{eff}}(\alpha; \Delta r_i)$, with $i = 1, 2$, obtained via the WI method nicely 'sit' on the smooth curves of the related potential calculated via the reference method; this feature demonstrates the consistency of the two approaches.

Finally, we compare the energy profiles $\phi_{\text{eff}}(\alpha; \Delta r_i)$ with $i = 1, 2$, calculated via the reference method and via the WI method for a broader range of α-values. These energy profiles are obtained by cutting, for a given angle α, a slice through the potential energy landscape $\phi_{\text{eff}}(\alpha; \Delta x, \Delta y)$ along selected lines in the $(\Delta x, \Delta y)$ plane. Our arbitrary choice for these lines are marked in Figure 10 by red and green dashed lines. In Figure 11 we show the energy profiles for $\alpha = 0°, 15°, 30°, 45°$, and $60°$. Again we find an excellent agreement between the results for $\phi_{\text{eff}}(\alpha; \Delta r_i)$ with $i = 1, 2$, obtained via the two aforementioned methods: the
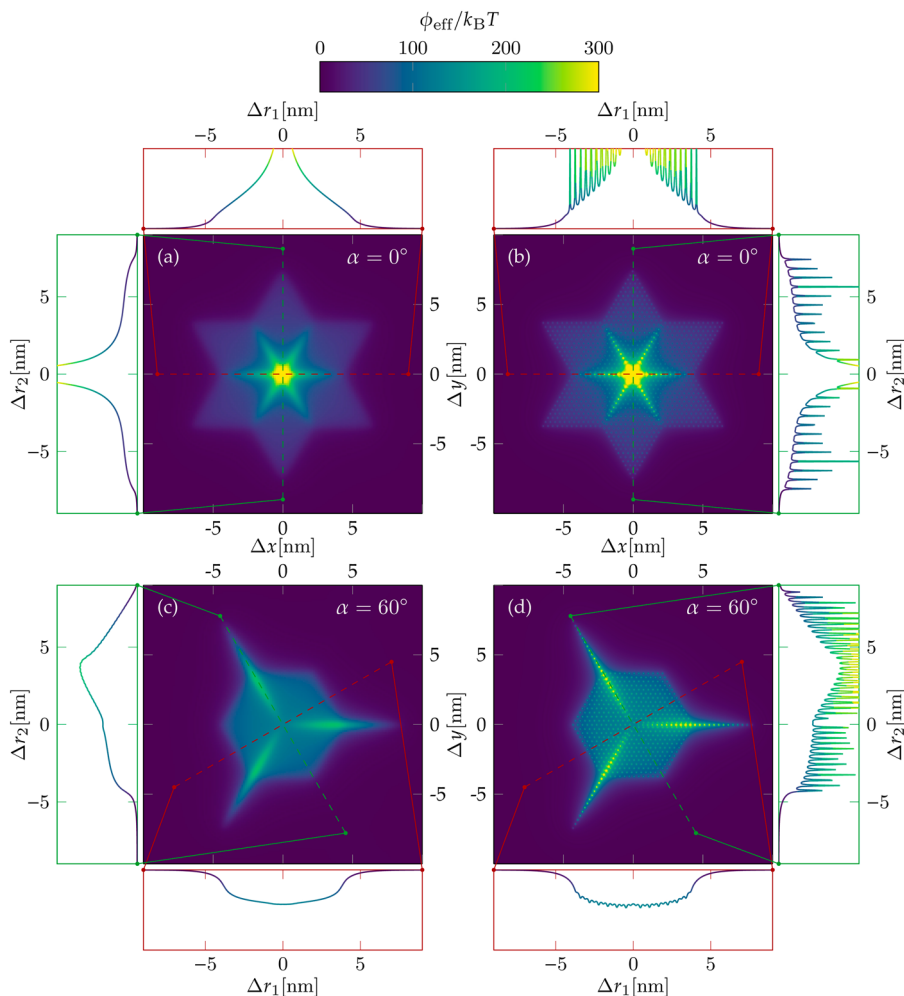

Figure 9. Illustration of the effective interaction parameters between rigid DNA stars in the flat configuration: displacements Δx and Δy and rotation angle α.

Figure 10. Effective potential, $\phi_{\text{eff}}(\alpha; \Delta x, \Delta y)$, between two flat DNA-stars with *rigid* junction in a contour plot as a function of the centre-of-mass shift Δx and Δy and the relative angle α between the two stars (see Figure 9). $\phi_{\text{eff}}(\alpha; \Delta x, \Delta y)$ is given in units of $k_B T$ (see also colour code at the top of the figure), whereas Δx and Δy are given in nm; α is indicated in the top-right corner of each panel. The interarm angles are fixed to $\theta_i = \frac{2\pi}{3}i$, with $i = 1, 2, 3$. In each of the panels two dashed lines (coloured in red and green) indicate two slices through the energy landscape of $\phi_{\text{eff}}(\Delta x, \Delta y)$. The energy profiles along these slices (in slice coordinates Δr_1 and Δr_2) are shown in the corresponding red- and green-framed plots. The data for the potentials were obtained *via* the reference method [43] (panels (a) and (c)) and *via* the WI method (panels (b) and (d)).

characteristic peaks of the WI-based data nicely 'sit' on the smooth curves obtained *via* the reference method. Again, these periodically arranged peaks are induced by the bead structure of our macromolecule, as discussed before.

3.2. Planar DNA stars with flexible junction

We have also calculated the effective potentials for flat stars with *flexible* junction. Of course, for this case no results obtained *via* the reference method are available. Here, the DNA arms are not completely straight and the interarm angles deviate from the ideal values $\theta_i = \frac{2\pi}{3}i$, $i = 1, 2, 3$, thus entropy plays an important role in the calculation of the effective potential. In order to calculate

the effective interactions between two stars, we tag one arm per DNA star to define the rotation angle α between the two stars as the angle between the corresponding arm vectors; the arm vector points from the first to the last monomer of the tagged arm. In contrast to rigid DNA stars, the fluctuations in the conformations of the (equilibrated) DNA stars require now a large number of Widom insertions to average over 2000 pairs of configurations.

The resulting effective potentials are shown in Figure 12 with the centre-of-mass position $\mathbf{r}_{\text{com}}$ as the effective coordinate of the star; results for $\alpha = 0°$ and $\alpha = 60°$ are depicted. As a consequence of the flexibility of the stars the effective potentials are now continuous functions of their variables, a fact which is both visible in the contour plots as well as in the energy profiles,
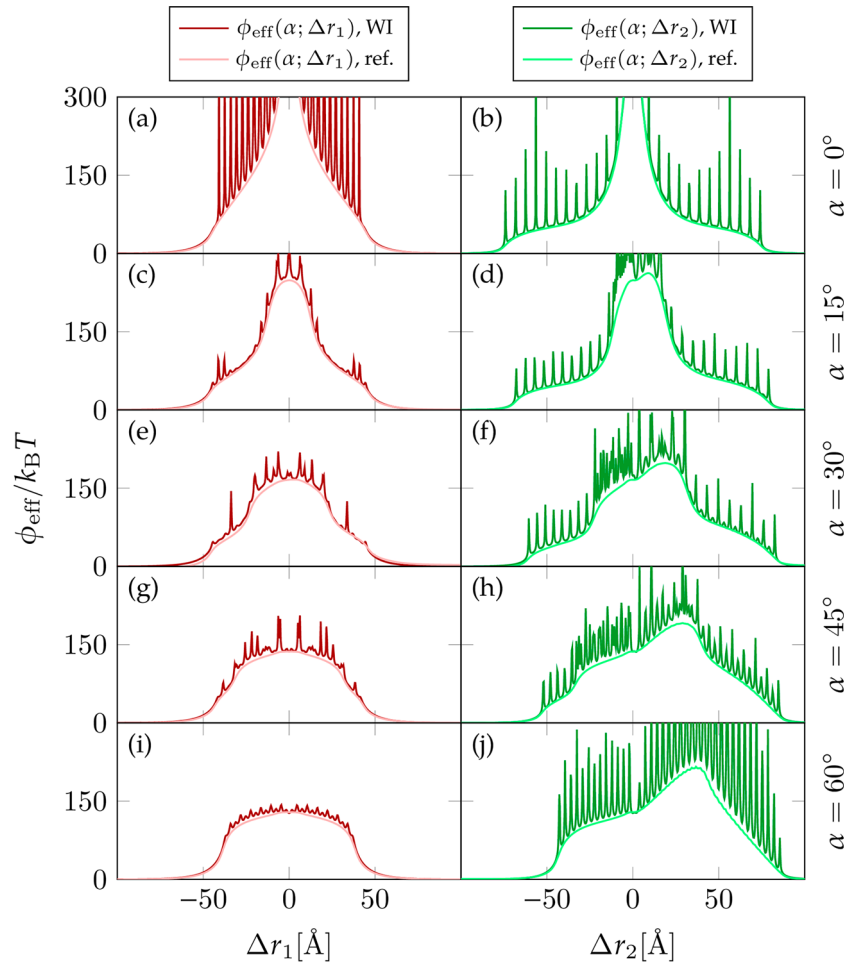
Figure 11. Energy profiles $\phi_{\text{eff}}(\alpha; \Delta r_1)$ and $\phi_{\text{eff}}(\alpha; \Delta r_2)$ of slices through the energy landscapes of the effective potentials $\phi_{\text{eff}}(\alpha; \Delta x, \Delta y)$ as functions of slice coordinates Δr_1 and Δr_2. The profiles are given in units of $k_B T$, whereas Δr_1 and Δr_2 are given in Å. Panels (a) to (j) show results obtained for rotation angles $\alpha = 0°$, $15°$, $30°$, $45°$, and $60°$ (as labelled). For each value of α the results for $\phi_{\text{eff}}(\alpha; \Delta r_i)$ ($i = 1, 2$) are shown for two different slices, which correspond to the dashed lines coloured red and green in Figure 10. Data were obtained *via* the Widom insertion method (labeled 'WI') and the reference method [43] (labeled 'ref').

obtained as slices through this two-dimensional energy landscape. The fingerprints of the granular internal bead-structure of the arms, that is present in the system of planar stars with rigid junctions, Figures 10 and 11, have been completely smeared out.

This insight shows how the introduced minimal flexibility in the model significantly modifies the effective potential of the system. The similar flexibility-induced sensitivity of the effective interaction between all-DNA constructs was also observed in the system of all-DNA dendrimers of the second generation [31] where it was shown how the effective interaction can be fine-tuned with user-prescribed insertion of short flexible segments between stiff DNA arms which further makes strong impact on self-assembly behaviour. The control over self-organisation of DNA constructs in solutions through programmable construction of macromolecules is an application-relevant feature that requires more detailed investigations. These results for the effective potential can

serve for further study of phase diagram of DNA stars in the confinement.

4. Conclusions

In this contribution, we have investigated the self-organisation scenarios of planar and of tripod-shaped all-DNA stars which are fixed via amphiphilic units to an air-water interface: in the planar configurations the entire arms are fixed to this interface while in the tripod configurations, the central monomer of the star is allowed to dive into the water with dissolved monovalent salt. The investigations are based on monomer-resolved simulation with suitable interactions between the beads that have been employed to mimic the structural properties of double-stranded DNA chain. By systematically increasing the planar packing fraction η_s in range from low to mid star densities, we have investigated the static
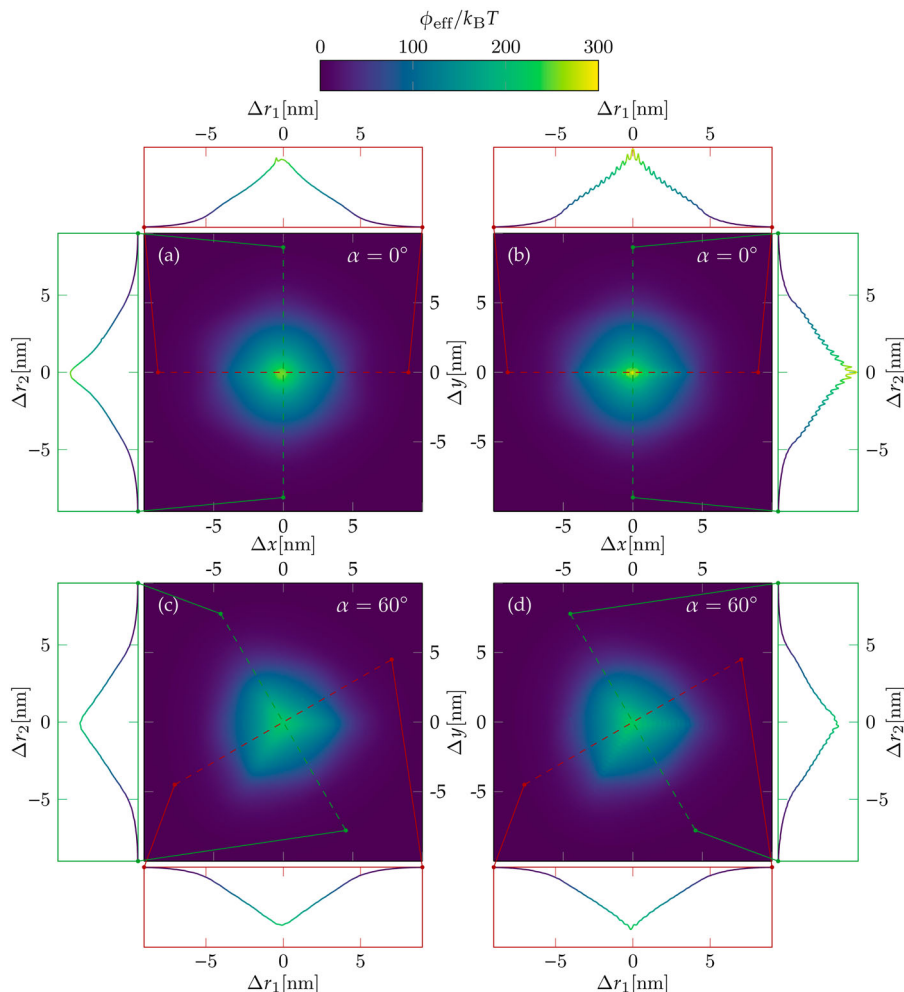
Figure 12. Effective potential $\phi_{\text{eff}}(\alpha; \Delta x, \Delta y)$ between two flat DNA stars with *flexible* junction in a contour plot as a function of the centre-of-mass shift Δx and Δy and the relative angle α between the two stars. $\phi_{\text{eff}}(\alpha; \Delta x, \Delta y)$ is given in units of $k_B T$ (see the colour code at the top of the figure), whereas Δx and Δy are given in nm; α is indicated in the top-right corner of each panel. In each of the panels, two dashed lines (coloured in red and green) indicate two slices through the energy landscape of $\phi_{\text{eff}}(\alpha; \Delta x, \Delta y)$. The energy profiles along these slices (in slice coordinates Δr_1 and Δr_2) are shown in the corresponding red- and green-framed plots. The data for the potentials were obtained *via* the WI method.

and dynamic properties of 2D assembly of all-DNA stars for both configurations.

For the planar configuration of DNA stars investigations could be carried out up to $\eta_s \simeq 0.34$. The radial distribution function shows the typical features of a disordered system; the logarithmic derivative of the mean squared displacement of the star centres reaches values that go down to $\chi(\Delta t) \simeq 0.8$ between the ballistic ($\chi(\Delta t) = 2$) and the diffusive ($\chi(\Delta t) = 1$) regimes. Comparing the time-scales of the auto-correlation function of the arms and of the mean squared displacement we can conclude that the orientational correlations decay faster than the spatial correlations.

In contrast to the planar configurations, the DNA stars in the tripod configuration have an additional degree of freedom, namely the vertical position of their central junction, which increases upon dipping the star

into solvent, shrinking in that way the area spanned by the ending beads of the three arms of a star. That enables denser stars packing in the confinement, so the simulations were extended up to $\eta_s \simeq 0.58$ in this case. From low to mid densities, DNA stars in tripod configuration show an almost identical behaviour as it is the case for the planar DNA stars, whereas for the highest densities, we find an emerging side-shoulder of the main peak in the radial distribution function, indicating the emergence of a supercooled structure.

Particular focus has been put on the probability distributions of the immersion depth of the central monomer, Δz, and of the angle enclosed by the arms and the air-water interface, ξ. As we vary η_s, we find a striking change in the shape of both distribution functions: for small densities the stars prefer to assume flat tripod configurations

while at high densities the stars assume rather sharp tripod configuration, induced by the competition between available space and steric repulsion. In the intermediate density regime, a broad variety of tripod configurations can be found, reflected by rather flat distributions of Δz and ξ. This consequently leads to the cause for obtained similar self-assembly patterns of two systems studied.

The experimental verification of results for the system at hand is still lacking, nevertheless, recently, 2D self-assembly of blunt-ended all-DNA 3-arms stars has been investigated in experiment [24]. The set up is restricted to the assembly on a supported lipid bilayers with cholesterol-mediated DNA anchoring. The research showed the importance of the interaction between DNA duplexes through π-stacking that leads to a long range order in controlled patterned surfaces. That opens the direction in which our further research of denser DNA stars solutions can be conducted to include the interaction between blunt-ends of DNAs that are not neglectable in dense environment and which is not present in our present bead-spring model.

To overcome restrictions of monomer-resolved simulations for studying denser DNA star solutions, one can employ the method of effective interactions and predict theoretically the corresponding phase behaviour. We paved the way for the proposed study by calculating the effective interactions between planar DNA stars, Section 3. In this paper, the emphasis is put on the comparison with the analytically obtained results for similar system of Y-shaped DNA stars [43]. As we have shown good agreement between two models, one can proceed with calculation of effective interaction for the tripod configuration of DNA star and show how the two systems compare in the regime of densities that are not accessible in full monomer-resolved simulations.

Disclosure statement

No potential conflict of interest was reported by the author(s).

Funding

ORCID

Nataša Adžić 🔘 http://orcid.org/0000-0003-4189-4410
Emmanuel Stiakakis 🔘 http://orcid.org/0000-0002-3845-3684
Christos N. Likos 🔘 http://orcid.org/0000-0003-3550-4834

References

[1] N.C. Seeman, Annu. Rev. Biochem. **79**, 65–87 (2010). doi:10.1146/biochem.2010.79.issue-1

[2] P.W. Rothemund, Nature **440** (7082), 297–302 (2006). doi:10.1038/nature04586

[3] Y. He, Y. Chen, H. Liu, A.E. Ribbe and C. Mao, J. Am. Chem. Soc. **127** (35), 12202–12203 (2005). doi:10.1021/ja0541938

[4] Y. Yonamine, K. Cervantes-Salguero, K. Minami, I. Kawamata, W. Nakanishi, J.P. Hill, S. Murata and K. Ariga, Phys. Chem. Chem. Phys. **18** (18), 12576–12581 (2016). doi:10.1039/C6CP01586G

[5] L. Liu, Z. Li, Y. Li and C. Mao, J. Am. Chem. Soc. **141** (10), 4248–4251 (2019). doi:10.1021/jacs.9b00843

[6] I.V. Martynenko, V. Ruider, M. Dass, T. Liedl and P.C. Nickels, ACS Nano **15** (7), 10769–10774 (2021). doi:10.1021/acsnano.1c04297

[7] H.N. Barad, H. Kwon, M. Alarcón-Correa and P. Fischer, ACS Nano **15** (4), 5861–5875 (2021). doi:10.1021/acsnano.0c09999

[8] Z. He, K. Shi, J. Li and J. Chao, Iscience **26** (5), 106638 (2023). doi:10.1016/j.isci.2023.106638

[9] Y. He, Y. Tian, A.E. Ribbe and C. Mao, J. Am. Chem. Soc. **128** (39), 12664–12665 (2006). doi:10.1021/ja065467+

[10] S. Howorka, Langmuir **29** (24), 7344–7353 (2013). doi:10.1021/la3045785

[11] K. Cervantes-Salguero, Y.A. Gutiérrez Fosado, W. Megone, J.E. Gautrot and M. Palma, Molecules **28** (9), 3686 (2023). doi:10.3390/molecules28093686

[12] Y. Yang, J. Wang, H. Shigematsu, W. Xu, W.M. Shih, J.E. Rothman and C. Lin, Nat. Chem. **8** (5), 476–483 (2016). doi:10.1038/nchem.2472

[13] P. Chidchob, D. Offenbartl-Stiegert, D. McCarthy, X. Luo, J. Li, S. Howorka and H.F. Sleiman, J. Am. Chem. Soc. **141** (2), 1100–1108 (2018). doi:10.1021/jacs.8b11898

[14] S. Agarwal, M.A. Klocke, P.E. Pungchai and E. Franco, Nat. Commun. **12** (1), 3557 (2021). doi:10.1038/s41467-021-23850-1

[15] Z. Deng and C. Mao, Angew. Chem. **116** (31), 4160–4162 (2004). doi:10.1002/ange.v116:31

[16] Z. Jin, W. Sun, Y. Ke, C.J. Shih, G.L. Paulus, Q. Hua Wang, B. Mu, P. Yin and M.S. Strano, Nat. Commun. **4** (1), 1663 (2013). doi:10.1038/ncomms2690

[17] X. Zhang, C. Gong, O.U. Akakuru, Z. Su, A. Wu and G. Wei, Chem. Soc. Rev. **48** (23), 5564–5595 (2019). doi:10.1039/C8CS01003J

[18] W. Wang, S. Yu, S. Huang, S. Bi, H. Han, J.R. Zhang, Y. Lu and J.J. Zhu, Chem. Soc. Rev. **48** (18), 4892–4920 (2019). doi:10.1039/C8CS00402A

[19] X. Sun, S. Hyeon Ko, C. Zhang, A.E. Ribbe and C. Mao, J. Am. Chem. Soc. **131** (37), 13248–13249 (2009). doi:10.1021/ja906475w

[20] R.J. Kershner, L.D. Bozano, C.M. Micheel, A.M. Hung, A.R. Fornof, J.N. Cha, C.T. Rettner, M. Bersani, J. Frommer, P.W. Rothemund and G.M. Wallraff, Nat. Nanotechnol. **4** (9), 557–561 (2009). doi:10.1038/nnano.2009.220

[21] B. Maier and J.O. Rädler, Phys. Rev. Lett. **82** (9), 1911 (1999). doi:10.1103/PhysRevLett.82.1911

[22] A. Aghebat Rafat, T. Pirzer, M.B. Scheible, A. Kostina and F.C. Simmel, Angew. Chem. Int. Ed. **53** (29), 7665–7668 (2014). doi:10.1002/anie.v53.29

[23] Y. Suzuki, M. Endo and H. Sugiyama, Nat. Commun. **6** (1), 8052 (2015). doi:10.1038/ncomms9052

[24] N. Avakyan, J.W. Conway and H.F. Sleiman, J. Am. Chem. Soc. **139** (34), 12027–12034 (2017). doi:10.1021/jacs.7b06572

[25] S. Kempter, A. Khmelinskaia, M.T. Strauss, P. Schwille, R. Jungmann, T. Liedl and W. Bae, ACS Nano **13** (2), 996–1002 (2018). doi: 10.1021/acsnano.8b04631

[26] N.C. Seeman, J. Theor. Biol. **99** (2), 237–247 (1982). doi:10.1016/0022-5193(82)90002-9

[27] Y. Li, Y.D. Tseng, S.Y. Kwon, L. d'Espaux, J.S. Bunch, P.L. McEuen and D. Luo, Nat. Mater. **3** (1), 38–42 (2004). doi:10.1038/nmat1045

[28] C. Jochum, N. Adžić, E. Stiakakis, T.L. Derrien, D. Luo, G. Kahl and C.N. Likos, Nanoscale **11** (4), 1604–1617 (2019). doi:10.1039/C8NR05814H

[29] P.S. Crozier and M.J. Stevens, J. Chem. Phys. **118** (8), 3855–3860 (2003). doi:10.1063/1.1540098

[30] A. Wynveen and C.N. Likos, Soft Matter **6** (1), 163–171 (2010). doi:10.1039/B919808C

[31] N. Adžić, C. Jochum, C.N. Likos and E. Stiakakis, Small **20** (21), 2308763 (2024). doi:10.1002/smll.v20.21

[32] S. Biffi, R. Cerbino, F. Bomboi, E.M. Paraboschi, R. Asselta, F. Sciortino and T. Bellini, Proc. Natl. Acad. Sci. **110** (39), 15633–15637 (2013). doi:10.1073/pnas.1304632110

[33] M. Siavashpouri, C.H. Wachauf, M.J. Zakhary, F. Praetorius, H. Dietz and Z. Dogic, Nat. Mater. **16** (8), 849–856 (2017). doi:10.1038/nmat4909

[34] E. Stiakakis, N. Jung, N. Adžić, T. Balandin, E. Kentzinger, U. Rücker, R. Biehl, J.K. Dhont, U. Jonas and C.N. Likos, Nat. Commun. **12** (1), 7167 (2021). doi:10.1038/s41467-021-27412-3

[35] E. Locatelli, P.H. Handle, C.N. Likos, F. Sciortino and L. Rovigatti, ACS Nano **11** (2), 2094–2102 (2017). doi:10.1021/acsnano.6b08287

[36] J.M. Parikka, K. Sokołowska, N. Markešević and J.J. Toppari, Molecules **26** (6), 1502 (2021). doi:10.3390/molecules26061502

[37] M. Kwak and A. Herrmann, Chem. Soc. Rev. **40** (12), 5745–5755 (2011). doi:10.1039/c1cs15138j

[38] C. Dohno, S. Makishi, K. Nakatani and S. Contera, Nanoscale **9** (9), 3051–3058 (2017). doi:10.1039/C6NR07084A

[39] A. Arnold, O. Lenz, S. Kesselheim, R. Weeber, F. Fahrenberger, D. Roehm, P. Košovan and C. Holm, in *Meshfree Methods for Partial Differential Equations VI*, (Springer, Berlin, 2013), pp. 1–23.

[40] W. Götze and L. Sjögren, Rep. Prog. Phys. **55** (3), 241 (1992). doi:10.1088/0034-4885/55/3/001

[41] P. Gallo, F. Sciortino, P. Tartaglia and S.H. Chen, Phys. Rev. Lett. **76** (15), 2730 (1996). doi:10.1103/PhysRevLett.76.2730

[42] P.G. Debenedetti and F.H. Stillinger, Nature **410** (6825), 259–267 (2001). doi:10.1038/35065704

[43] C.A. Velasco, C.N. Likos and G. Kahl, Mol. Phys. **113** (17–18), 2699–2706 (2015). doi:10.1080/00268976.2015.1048318

[44] B.M. Mladek and D. Frenkel, Soft Matter **7** (4), 1450–1455 (2011). doi:10.1039/C0SM00815J

[45] R. Blaak, B. Capone, C.N. Likos and L. Rovigatti, in *Computational Trends in Solvation and Transport in Liquids-Lecture Notes*, 28 vols. (Forschungszentrum Julich, Julich, 2015), pp. 209–258.

Appendix. Simulation details

The Y-shaped DNA star is approximated with the bead-spring model used in [28] where each nucleotide is represented by a monomer of mass $m = 660$ u, size $d = 18$ Å and charge $q = -e$ that interacts with the Hamiltonian:

$$H_{mm} = V_{ster} + V_b + V_{bend} + V_{el}. \quad (A1)$$

The steric interaction between monomer beads takes the form

$$V_{ster}^{mm} = 4\epsilon \left[\left(\frac{\sigma}{r - r_{mm}} \right)^{12} - \left(\frac{\sigma}{r - r_{mm}} \right)^6 + \frac{1}{4} \right] \quad \text{if} \quad r_{mm} \leq r \leq \sqrt[6]{2}\sigma + r_{mm} \quad (A2)$$

otherwise for $r < r_{mm}$ it diverges, while it vanishes for $r > \sqrt[6]{2}\sigma + r_{mm}$. The input parameters are $\sigma = 4$ Å and $\epsilon = 1$ kJmol^{-1} and $r_{mm} = 2r_m - \sigma$, with $r_m = 9$ Å being the radius of monomer, so that the steric interaction acts in the range $r < 18.5$ Å corresponding to the effective diameter of the DNA helix.

The harmonic bonding potential is given

$$V_b = \frac{k_b}{2}(r - l_b)^2 \quad (A3)$$

with the spring constant $k_b = 210$ kJ(molÅ^2)$^{-1}$ and equilibrium bond length $l_b = 3.4$ Å.

The harmonic bending angle potential models the stiffness of a DNA arm by acting on the angle ϕ between bonds connecting neighbouring monomers:

$$V_{bend} = \frac{k_\phi}{2}(\phi - \pi)^2 \quad (A4)$$

with bending energy $k_\phi = 750$ kJmol^{-1} chosen to reproduce the typical persistence length of double-stranded DNA chain. The central junction is left fully flexible by setting the bending energy to zero.

All DNA stars systems are studied in high salt concentration, $c = 100$ mM, allowing counterions and salt ions to be implicitly treated through Debye length κ^{-1}. Hence, the electrostatic interaction between charged monomer beads is modelled via a Debye-Hückel interaction

$$\frac{V_{el}(r)}{k_B T} = \frac{q^2}{4\pi \epsilon_0 \epsilon} \frac{e^{-\kappa r}}{r} \quad (A5)$$

with $\kappa = 0.106$ Å^{-1}. The dielectric constant of both media water and air is set to $\epsilon = 80$ assuming that electrostatic effect that arise when the dielectric jump is present in the system can be neglected as subdominant in the case of high salt concentration.

The bulk 2D solutions of both planar and tripod DNA stars are simulated using two-steps procedure. First the system is warmed up using $N_{steps} = 10^5$ simulation steps with time step $\Delta t = 10^{-15}$ s for a total simulation time $t = 10^{-10}$ s

and then simulated for $N_{\text{steps}} = 2 \times 10^7$ simulation steps with time step $\Delta t = 5 \times 10^{-15}$ s for a total simulation time $t = 10^{-7}$ s for all area densities η_{s}. Simulations were run in canonical NVT ensembles with periodic boundary conditions at $T = 298$ K using a Langevin thermostat. The number of stars is kept fixed to 400 units (resulting in 15600 monomers) and the length of the quadratic simulation cell is varied to achieve the following densities of the solutions $\eta_{\text{s}} = 0.17, 0.20, 0.24, 0.27, 0.31$ and 0.34 corresponding to the cell length $l = (2.19, 2.00, 1.85, 1.73, 1.63,$ and $1.55) \times 10^3$ Å respectively. Tripod DNA stars solutions are considered for additional star densities: $\eta_{\text{s}} = 0.37, 0.41, 0.44, 0.48, 0.51, 0.54,$ and 0.58, setting the cell length $l = (1.48, 1.41, 1.36, 1.31, 1.26, 1.22,$ and $1.19) \times 10^3$ Å accordingly.